The Role of Clear-Sky Identification in the Study of Cloud Radiative Effects: Combined Analysis from ISCCP and the Scanner of Radiation Budget

C. J. STUBENRAUCH AND V. BRIAND

Laboratoire de Météorologie Dynamique, Ecole Polytechnique, Palaiseau, France

W. B. ROSSOW

NASA Goddard Institute for Space Studies, New York, New York

(Manuscript received 1 February 2001, in final form 28 October 2001)

ABSTRACT

Two additional narrowband channels of the Scanner of Radiation Budget (ScaRaB) instrument should improve the Earth Radiation Budget Experiment (ERBE) cloud scene identification. Applying the original International Satellite Cloud Climatology Project (ISCCP) algorithms to the ScaRaB narrowband data gives a clear-sky frequency that is about 5% lower than that given by quasi-simultaneous ISCCP data, an indication that the ISCCP cloud detection is very stable. However, one would expect about 10%–20% smaller clear-sky occurrence for the larger ScaRaB pixels. Adapting the ISCCP algorithms to the ScaRaB spatial resolution and to the different time sampling of the ScaRaB data leads to a reduction of residual cloud contamination. A sensitivity study with time–space-collocated ScaRaB and ISCCP data shows that the clear-sky identification method has a greater effect on the clear-sky frequency and therefore on the statistics than on the zonal mean values of the clear-sky fluxes. The zonal outgoing longwave (LW) fluxes corresponding to ERBE clear sky are in general about 2–10 W m^{-2} higher than those from the ScaRaB-adapted ISCCP clear-sky identifications. The latter are close to fluxes corresponding to clear-sky regions from ISCCP data, whereas ScaRaB clear-sky LW fluxes obtained with the original ISCCP identification lie about 1–2 W m^{-2} below. Especially in the Tropics, where water vapor abundance is high, the ERBE clear-sky LW fluxes seem to be systematically overestimated by about 4 W m^{-2}, and shortwave (SW) fluxes are lower by about 5–10 W m^{-2}. However, another source of uncertainty in the monthly mean zonal cloud radiative effects comes from the low frequency of clear-sky occurrence, when averaging over regions that correspond to the spatial resolution of general circulation models. An additional systematic sampling bias in the clear-sky fluxes appears because the clear-sky regions selected by the different algorithms occur in different geographic regions with different cloud properties.

1. Introduction

Clouds have an important impact on the energy distribution in the atmosphere mainly through two mechanisms: on one hand they cool the earth (mostly the surface) by reflecting solar radiation, and on the other hand they warm the earth (mostly the atmosphere) by partially capturing emitted thermal radiation. A first estimation of the importance of these effects was determined by comparing incoming and outgoing fluxes at the top of the atmosphere (TOA) between all situations and monthly averaged clear-sky situations in the same regions (Charlock and Ramanathan 1985). The Earth Radiation Budget Experiment (ERBE; Barkstrom et al. 1989) has shown that, in the global annual mean, clouds cool the earth by about 20 W m^{-2} (Harrison et al. 1990). However, regional and seasonal radiative effects of clouds can be quite different, depending on their physical properties (cf. Stephens and Greenwald 1991; Ockert-Bell and Hartmann 1992; Stubenrauch et al. 1999; Chen et al. 2000). As the geographical and temporal distributions of the radiative fluxes at TOA are directly linked to the global circulation of the atmosphere and oceans, the difference between clear-sky and cloudy fluxes has been widely used to test the realism of climate models (cf. Cess and Potter 1987; Harshvardhan et al. 1989; Ridout et al. 1994). Therefore, a reliable identification of clear-sky situations is important. Several studies (Hartmann and Doelling 1991; Rossow and Zhang 1995; Collins and Inamder 1995; Stubenrauch et al. 1997; Chen et al. 2000) suggest that ERBE clear-sky longwave (LW) fluxes tend to be biased high, especially in tropical regions where atmospheric water vapor is abundant.

The Scanner of Radiation Budget (ScaRaB) radiometer on board the Russian *Meteor-3/07* satellite provided measurements of reflected solar radiation and

Corresponding author address: Claudia J. Stubenrauch, Laboratoire de Météorologie Dynamique, Ecole Polytechnique, F-91128 Palaiseau cédex, France.
E-mail: stubenrauch@lmd.polytechnique.fr

emitted thermal radiation at TOA from March 1994 to February 1995 with ERBE-like broadband LW and shortwave (SW) channels (Viollier et al. 1995; Kandel et al. 1998). The inclination of the orbit (82.6°) is such that all local hours are observed within 104 days. Measured broadband radiances are currently converted into radiative fluxes by the ERBE inversion algorithm (Smith et al. 1986). Scene-dependent angular corrections play an important part in this inversion. A reliable scene identification is not only important for the angular dependence models (ADMs), but also for studying cloud radiative effects, as explained above. Two additional ScaRaB narrowband channels, centered on the 11.5-μm infrared (IR) atmospheric window and on the 0.6-μm visible (VIS) band, should allow an improvement of the cloud scene identification because the contrast between clouds and clear sky is larger for these narrowband channels than for the broadband channels.

A regional study (Stubenrauch et al. 1996) has already shown that the ScaRaB narrowband channels make it possible, even at the relatively low ScaRaB spatial resolution of about 60 km (at nadir), to establish a more detailed cloud-field identification than with the ERBE method. On the other hand, in order to obtain a cloud-scene identification, which is reliable over the whole globe it is better to start from already developed cloud detection algorithms that are functioning globally.

The International Satellite Cloud Climatology Project (ISCCP) method for cloud detection and determination of cloud and surface properties makes use of the same narrowband channels as ScaRaB, but is applied to a collection of measurements at a better spatial resolution of about 5 km, from geostationary and polar orbiting satellites around the globe (Rossow and Schiffer 1991, 1999). Even if the initial spatial resolution of these measurements is much better, the ISCCP cloud detection method is a good starting point for an improved ScaRaB scene identification. Therefore, this method was applied to the ScaRaB VIS and IR radiances for cloud detection and for the determination of their properties.

Four different clear-sky identification methods are described in section 2. In sections 2a and 2b, respectively, the original ERBE and ISCCP clear-sky identifications are briefly recalled. The thresholds of the original ISCCP algorithm are then adjusted to account for the ScaRaB reduced spatial resolution (section 2c). In section 2d we present an algorithm that also takes into account the different time sampling of the ScaRaB data. In this algorithm clear-sky reference radiances are determined from regional statistics of the same geotype instead of using time statistics from the same location as in the ISCCP algorithm. Section 3 compares results on clear-sky frequencies and clear-sky LW fluxes at TOA obtained with these four clear-sky identification methods. A sensitivity study with time–space-collocated ScaRaB and ISCCP data evaluates the effects of clear-sky identification method and of statistical averaging on clear-sky frequency and on clear-sky fluxes at TOA. Section 4 discusses the effect of clear-sky statistics on cloud radiative effects. Conclusions are given in section 5.

2. Clear-sky identification methods

a. ERBE scene identification

The ERBE scene identification (Wielicki and Green 1989) is based on a maximum likelihood method applied to the broadband LW and SW radiances. Scenes are grouped into four different classes depending on cloud cover: from clear sky, which is described by the warmest and darkest scenes; over partly cloudy and mostly cloudy to overcast, which is described by the coldest and brightest scenes. Kernels that vary with latitude and season for these scenes have been predetermined for five different background geotypes (ocean, land, desert, coast, and snow); see Hartmann and Doelling (1991) for a discussion about the effects of kernels that are constant for whole seasons. This cloud scene identification is used to choose the angular dependence models for the conversion of radiances into fluxes. The ERBE clear-sky identification has also been extensively used for the study of cloud radiative effects.

b. ISCCP cloud detection

ISCCP cloud detection and classification is based on a series of variable threshold tests applied to narrowband IR and VIS radiances. These narrowband radiances exhibit a larger contrast between clouds and clear sky and are therefore better-suited for cloud detection than broadband radiances (cf. Rossow et al. 1989).

The ISCCP dataset gathers data from geostationary and polar satellites with an initial pixel resolution of about 4 to 7 km. Polar satellite data from the Advanced Very High Resolution Radiometer (AVHRR) are distributed in the Global Area Coverage (GAC) format, the initial spatial resolution of 1 km reduced to about 1 km $\times$ 4 km by averaging four pixels in a line and sampling every fifth line. These pixels are then sampled to a spatial interval of about 25 km. Clouds are detected through a final IR–VIS threshold test comparing the measured radiances to reference clear-sky radiances that have been determined from pixels that exhibit low IR spatial and temporal variability (Rossow and Garder 1993a). Therefore, the main part of the algorithm consists of the determination of reference clear-sky radiances (called ''clear-sky composite'' radiances in the ISCCP algorithm) for each pixel. In a first step, one determines the locally warmest pixels (within threshold $\Delta 1$ of 8 K over land and 3.5 K over ocean) over areas, which are about 100 km $\times$ 100 km over land (3 $\times$ 3 grid boxes) and vary over ocean from about 450 km $\times$ 450 km (15 $\times$ 15 grid boxes) in the Tropics to 270 km (latitude) $\times$ 750 km (longitude) (9 $\times$ 25 grid boxes) in the midlatitudes, in order to take into account the meridional surface temperature gradient. A second criterion for clear

TABLE 1. Modifications of thresholds in the different steps of the ISCCP cloud detection in order to adapt it for the ScaRaB spatial resolution. The temporal variability thresholds Δ2 and Δ3 decide whether the pixel is clear or cloudy/undetermined.

Algorithm part	Threshold	Original value		Value for ScaRab	
		Land	Ocean	Land	Ocean
Temporal variability test	Δ2 (K)	2.0	1.0	0.8	0.4
	Δ3 (K)	8.0	3.5	3.0	1.0
IR composite logic	Short term—Δ2 (K)	5.0	2.0	3.3	1.3
	Long term—Δ3 (K)	8.0	2.5	5.3	2.7
VIS composite logic	Short term—Δ2 (%)	6.0	3.0	4.0	2.0
	Long term—Δ3 (%)	3.5	1.5	2.3	1.0
Final thresholds	IR (K)	4.0	2.5	1.5	1.0
	VIS (%)	6.0	3.0	4.0	2.0

sky is a similar temperature (within threshold Δ2 of 2.0 K over land and 1.0 K over ocean) in comparison with values at the same location on the previous and the following day at the same time of day. The spatial variability threshold Δ1 labels a pixel either cloudy or undetermined, whereas the temporal variability thresholds Δ2 and Δ3 label a pixel either clear or cloudy/undetermined. In a next step, short- and long-term clear-sky statistics are collected respectively over 5 and 15 days for land areas and over 15 and 30 days for ocean areas. These results are then analyzed by taking into account the geotype variability characteristics to determine the clear-sky composite radiances. The final scene identification depends on a comparison of each measured radiance to its clear sky composite value. The different thresholds are summarized in Table 1.

Whereas the ERBE scene identification is applied to pixels with a size of about 60 km, the ISCCP algorithm has been developed for pixels with a size of about 4–7 km and sampled to intervals of 25 km. One ScaRaB pixel can be represented by about four ISCCP pixels, assuming that the sampling of the latter represents the characteristics of the whole region of 60 km × 60 km (Sèze and Rossow 1991). Differences in pixel size and in sampling between ScaRaB and the ISCCP data are illustrated in Fig. 1. These differences will particularly influence the spatiotemporal statistics used for the determination of clear-sky composites in the ISCCP algorithm, which will be studied in more detail in section 2c.

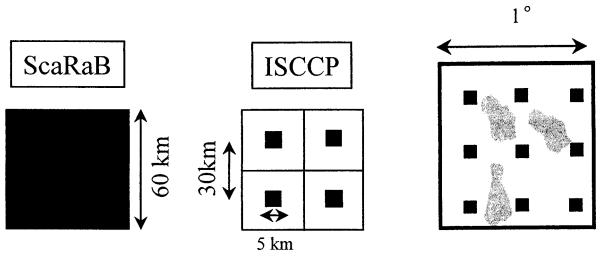

FIG. 1. Schematic view of a ScaRaB pixel and of sampled ISCCP pixels over an area corresponding to the size of a ScaRaB pixel to illustrate spatial resolution and sampling. Both datasets are space–time collocated at a spatial resolution of 1° (outer right scheme). The sampling of ISCCP can miss small clouds that occur between the measurements.

The original ISCCP algorithm has been applied to the whole ScaRaB dataset. The pixel data have been put onto a grid with a spatial resolution of 0.33°, corresponding to 1.33 times the initial spatial resolution of ISCCP data. ISCCP cloud detection and determination of cloud properties are then carried out the same way as for data from a polar orbiting satellite.

c. ISCCP cloud detection adapted to ScaRaB spatial resolution

For the following study, we match ISCCP pixel-level data from the *NOAA-12* AVHRR data in the GAC format to ScaRaB data. For the second half of March 1994, the observation time of both satellites was quite similar. From 24 to 26 March 1994 the crossing time at the equator was within a few minutes of 0730 LST. The observation time coincidence is best at low latitudes (<30°), because the two satellites, *Meteor-3/07* and *NOAA-12*, are orbiting the earth in opposite directions.

An increase of pixel size from 5 to 60 km leads to an increase of surface and cloud variability that is counteracted by effects of averaging over the larger pixel area. However, both effects serve to reduce the radiance contrast between cloudy and clear scenes, producing more cloud contamination in 60 km pixels labeled as clear than in 5 km pixels labeled as clear. This tendency is reinforced by an increasing probability for mixtures of cloud and clear scenes to occur within the larger pixel, especially for low-level clouds (cf. Wielicki and Parker 1992). To illustrate these effects for ocean areas, we first compare in Fig. 2 the IR brightness temperature distributions from the ISCCP data and from ScaRaB pixels of all scenes and of scenes identified as clear-sky. For a better comparison, each distribution has been normalized to its peak value. The standard deviation for all AVHRR pixels (Fig. 2a) is slightly higher than for ScaRaB pixels (Fig. 2c), by about 1.3 K, indicating that the averaging effect dominates the increased variability over this particular range of spatial scales. The mean values are, as expected, nearly the same. However, when considering only the clear-sky scenes, the standard deviation of ScaRaB clear-sky scenes (Fig. 2d) is slightly higher (by about 1.3 K) and the mean value slightly

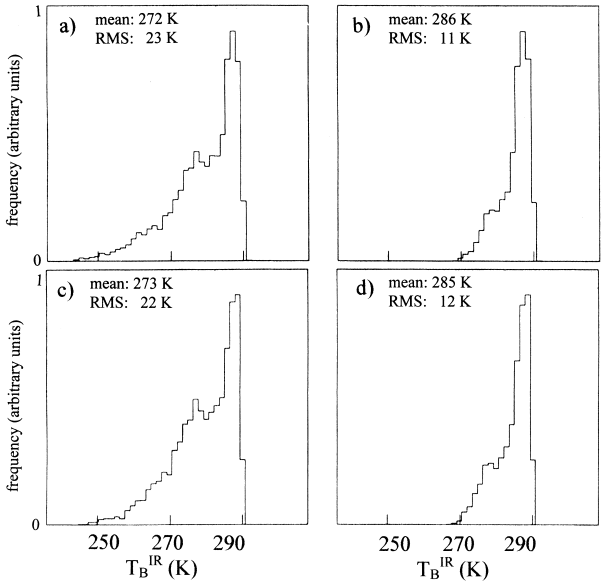

FIG. 2. Brightness temperature (T_B) distributions over ocean for (a) all ISCCP data, (b) only ISCCP clear-sky scenes from ISCCP data, (c) all ScaRaB data, and (d) only ISCCP clear-sky scenes from ScaRaB data. The distributions are shown in arbitrary units and have been normalized to the peak value. Mean values and std dev are also given.

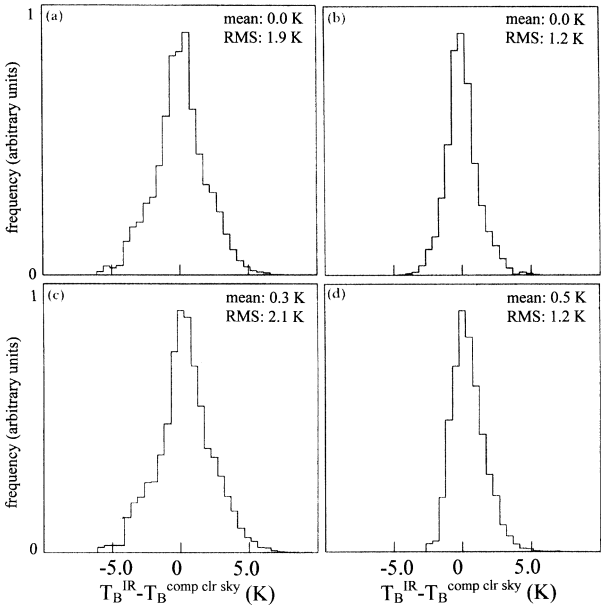

FIG. 3. Distributions of differences between clear-sky brightness temperatures and clear-sky composite brightness temperatures over ocean (a) for ISCCP data, (b) for simulated ScaRaB data (using four adjacent ISCCP grid boxes), (c) for ScaRaB data on which the original ISCCP cloud detection was applied, and (d) for ScaRaB data using spatial resolution–adapted thresholds for the clear-sky composite determination. The distributions are shown in arbitrary units and have been normalized to the peak value. Mean values and std dev are also given.

lower (by about 1.2 K), indicating a small additional cloud contamination of the ScaRaB pixels, which have been identified as clear-sky by the original ISCCP algorithm.

Since the absolute values of the clear-sky brightness temperature and reflectance also depend on the clear-sky statistics of different geographical regions, we compare the relative brightness temperatures and reflectance distributions, obtained by subtraction of the clear-sky composite values. The distribution of clear-sky brightness temperatures around the clear-sky composite in Fig. 3 should represent the spatial and temporal variability of the surface (Rossow and Garder 1993a,b). If one compares, in Figs. 3a and 3b, the distributions of the ISCCP data and of simulated ScaRaB pixels (by an accumulation of four adjacent ISCCP gridboxes, see Fig. 1), one can clearly see the expected decrease in surface variability of about 0.7 K due to averaging over the larger pixel size. Yet, one observes, in Fig. 3c, a larger standard deviation (by 0.2 K) of the distribution of ISCCP-detected clear sky over ScaRaB pixels than for the ISCCP data, reflecting increased cloud contamination.

The thresholds in the ISCCP cloud detection have to be adjusted so that the relative clear-sky brightness temperature distribution looks similar to the one for the simulated ScaRaB pixels in Fig. 3b. The algorithm adjustment must take into account that the spatial and temporal variability of the surface characteristics is smaller for the larger ScaRaB pixels. Therefore, thresholds used in the space–time variability test (the first part of the ISCCP algorithm) must be reduced. Since the test on spatial variability results only in a distinction between a cloudy and undetermined scene (Rossow and Garder 1993a) and since the behavior of spatial variability cannot be easily estimated, because the regions covering the same number of pixels are larger and therefore offset the decrease in variability, only the thresholds used in the temporal variability test are altered. These have been reduced to about 1/2 of their original values (Table 1).

The second part of the algorithm to be modified is the clear-sky composite radiance determination. The relation between the extremes and the average clear-sky radiances, specific to each geotype, depends again on the spatial resolution, either for short- or long-term statistics (Sèze and Rossow 1991; Rossow and Garder 1993a). Table 1 summarizes the new thresholds, which have been reduced to approximately 2/3 of their original values.

With these modifications a new distribution of clear-sky brightness temperatures around the clear-sky composite values is obtained, shown in Fig. 3d. The right side of the distribution, corresponding to the warmest pixels, now looks similar to the one for simulated ScaRaB pixels in Fig. 3b. This indicates that the clear-sky composite radiances are now adequate as a reference for scene identification. In the case of the visible radiances, the adjustment is more difficult because the

TABLE 2. Geotypes used to determine clear-sky composite radiances in a cloud detection adapted to the ScaRaB temporal sampling and their link to CERES/SARB scene types.

Geotype	CERES/SARB geotype
Evergreen forest	1, 2
Deciduous forest	3–5
Bushland	6, 7
Savanna	8, 9
Grasslands	10–14
Tundra	18
Desert	16
Partial snow/ice	ISCCP partial snow
Total snow/ice	15 and ISCCP total snow
Ocean	17

viewing geometry is not exactly the same because of the opposite orbits. Therefore, the adjustment of VIS thresholds is made by the same amount as the IR radiances, as shown in Table 1. After the final IR–VIS thresholds have been adjusted the entire distribution (not shown) now looks like the one for the four merged ISCCP gridboxes.

d. Cloud detection adapted to ScaRaB local time sampling

Another difference between the ISCCP data and ScaRaB data is the temporal sampling. The ISCCP cloud detection was initially developed for measurements on satellites that observe a given location at the same time of the day, allowing for precise statistics for the clear-sky composites (Rossow and Garder 1993b). Since the observation time of the *Meteor-3/07* satellite shifts by about 4 h over a month, the longer-term statistics of clear-sky composites could be more difficult to establish, especially for geographical regions (like deserts) where the diurnal cycle has a large amplitude. The ScaRaB observation time is explicitly presented for every month in Capderou (1995). During the month of March 1994, the observation time at the equator shifts from about 1030 LST to 0630 LST.

In order to take this time shift properly into account, a new algorithm has been developed in which clear-sky composite radiances are now determined from regional statistics of the same geotype instead of using time statistics (during 15 and 30 days, respectively, for short- and long-term statistics) for the same location.

1) DETERMINATION OF CLEAR-SKY COMPOSITES

The first step consists of defining a more detailed geotype classification than used by the original ISCCP algorithm, since for the determination of the clear-sky composite radiances it is necessary to compare the brightness temperatures and reflectances over regions for which one would expect a similar clear-sky behavior. On the other hand, the population of samples over the region must be large enough in order to assure the presence of a pixel with clear sky. Starting from the Cloud and the Earth's Radiant Energy System/Surface and Atmospheric Radiation Budget (CERES/SARB) geotype classification (Rutan and Charlock 1997), which includes 18 geotypes at a spatial resolution of 0.166°, we merge these into nine geotypes over land, presented in Table 2. Note that for the identification of snow- and ice-covered scenes, the ISCCP information is directly used in order to take into account seasonal variations. The geotype ''ocean'' is split into 12 30° longitude bands, leading to oceanic regions with similar airmasses. The final classification, consisting of 21 land and ocean types at a spatial resolution of 1°, represents a compromise between the sample size requirement and climatic homogeneity.

For each geotype, the clear-sky composites are determined as a function of latitude for IR and as a function of viewing geometry for VIS radiances. The reference values (maximum IR and minimum VIS radiances) will be determined over a short time period in order to eliminate effects due to the shift of the observation time.

First we study the importance of sample population for establishing stable reference clear-sky brightness

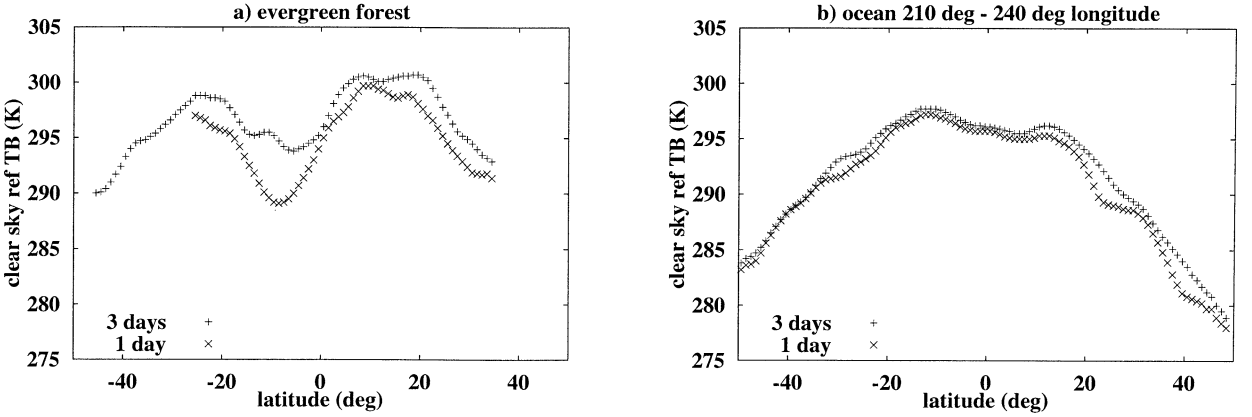

FIG. 4. Clear-sky reference brightness temperatures, obtained from different temporal statistics, as a function of latitude in Mar 1994 (a) for evergreen forest and (b) for ocean between 210° and 240° lon.

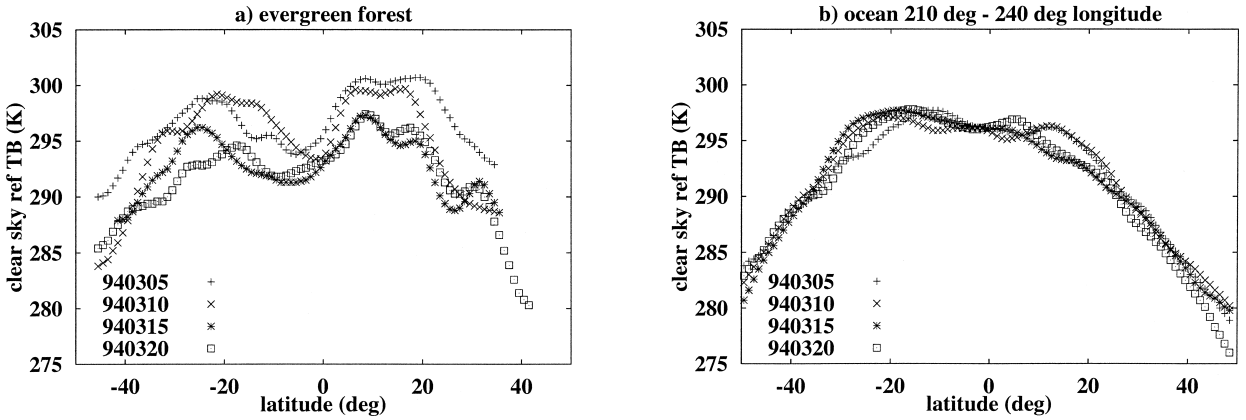

FIG. 5. Clear-sky reference brightness temperature as a function of latitude for four time periods corresponding to different observation times in Mar 1994 (a) for evergreen forest and (b) for ocean between 210° and 240° lon.

temperatures (or clear sky composites). If the sample size is not large enough, there is a risk that there is no clear-sky scene over the observed geotype. In this case, the maximum brightness temperature T_B^{ref} will correspond to a cloudy scene and be biased low. On the other hand, if the chosen geotype covers a region that is too large, T_B^{ref} corresponds just to the warmest subregion (for example caused by a marine current). In this case, the colder clear-sky scenes in the rest of the region would be considered cloudy. In the following, the effects of the width of the latitude band and of the length of the time period on the determination of the clear-sky IR composites are examined.

Figure 4 compares reference clear-sky brightness temperatures T_B^{ref} as a function of latitude obtained from statistics over a latitude band corresponding to three ScaRaB pixels (1°) over a time period of 1 day and 3 days. As an example, results are shown for evergreen forest and one ocean region. The maximum brightness temperature is only kept as T_B^{ref} if it came from a sample of more than nine values in order to reduce the probability of cloud contamination. Then, T_B^{ref} is smoothed and interpolated as a function of latitude for each geotype in order to eliminate values too far from the mean and to fill in the missing values.

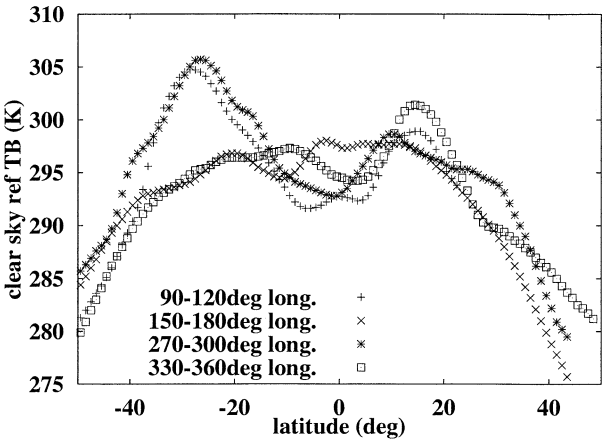

FIG. 6. Clear-sky reference brightness temperature as a function of latitude in Mar 1994 for four different lon bands of ocean.

The variation of T_B^{ref} due to the observation time shift of the *Meteor-3/07* satellite orbit is illustrated in Fig. 5, which shows T_B^{ref} as function of latitude for the same geotypes as in Fig. 4 at different time periods during March 1994. Statistics are collocated at each time over 3 days. One can see a decrease of T_B^{ref} of about 5–10 K within 15 days from 5 March (observation at 1000 LST) to 20 March 1994 (observation at 0730 LST).

From Figs. 4 and 5, one concludes that statistics over three days seems to be reasonable, because on the one hand in regions with frequent cloudiness, especially in the Tropics, T_B^{ref} could be easily underestimated by up to 5 K by using statistics of only 1 day, and on the other hand the observation time shift within 5 days can produce a change of 5 K in certain regions. The necessity of a more detailed ocean classification scheme into regions of restricted longitude is revealed in Fig. 6, showing zonal mean T_B^{ref} for 4 of the 12 ocean regions: At some latitudes, T_B^{ref} can vary by up to 10 K from one ocean region to the other.

In order to determine the VIS clear-sky composite radiances for each geotype, the minimum, within intervals of solar zenith angle, viewing zenith angles, and relative azimuth angles, is kept as the reference if it is obtained from a sample of more than nine values, and then the values are smoothed as in the case of the brightness temperatures but according to the different viewing/illumination angles instead of latitude.

2) DETERMINATION OF FINAL IR–VIS THRESHOLDS

Clear sky is identified by comparing 1) the measured brightness temperature T_B with the local maximum brightness temperature T_B^{9pix} over nine adjacent ScaRaB pixels and to T_B^{ref} (as function of latitude and geotype) and 2) the measured reflectance R_{VIS} with the local min-

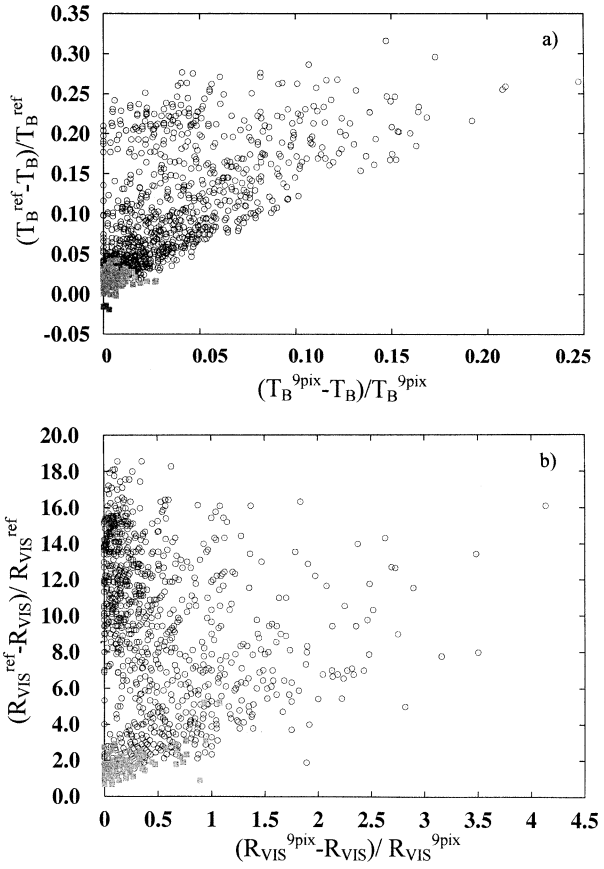

FIG. 7. Scatterplots of (a) relative brightness temperature difference compared with the reference and with the local maximum and (b) relative reflectance difference compared with the reference and with the local minimum. Gray squares correspond to clear-sky scenes identified by the ScaRaB spatial resolution adapted ISCCP cloud detection. Scene type is evergreen forest.

imum reflectance R_{VIS}^{9pix} over nine adjacent ScaRaB pixels and with the reference reflectance R_{VIS}^{ref} (as function of observation geometry and geotype). Step 2 can be applied only to daytime measurements. As an example, Fig. 7 shows scatterplots of these variables: (a) $(T_B^{9pix} - T_B)/T_B^{9pix}$ and $(T_B^{ref} - T_B)/T_B^{ref}$, and (b) $(R_{VIS}^{9pix} - R_{VIS})/R_{VIS}^{9pix}$ and $(R_{VIS}^{ref} - R_{VIS})/R_{VIS}^{ref}$ for the geotype evergreen forest. Pixels identified as clear-sky by the spatial resolution–adapted ISCCP algorithm described in section 2c have been marked as gray. These clear-sky scenes are well concentrated at low values of these four variables, whereas the cloudy pixels populate the space with larger values.

The relative thresholds are then determined for each geotype by comparing the distributions of these four variables to the distributions of the clear-sky scenes obtained from the adapted ISCCP algorithm. By setting the thresholds to the mean plus one standard deviation of these ISCCP clear-sky distributions, the agreement between both clear-sky identifications is about 85% (90% over the ocean). Agreement varies from 70% for bushland to 94% for evergreen forest. Even if we use the spatial resolution–adapted ISCCP clear-sky identi-

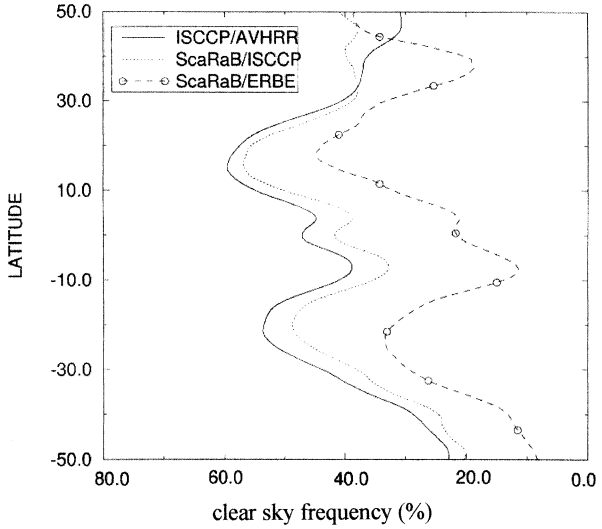

FIG. 8. Zonally averaged clear-sky frequency as determined by the ERBE identification (ScaRaB–ERBE) and by the original ISCCP cloud detection on ScaRaB pixels (ScaRaB–ISCCP) compared with clear-sky frequency from ISCCP data (AVHRR–ISCCP) at close observation time during the second half of Mar 1994.

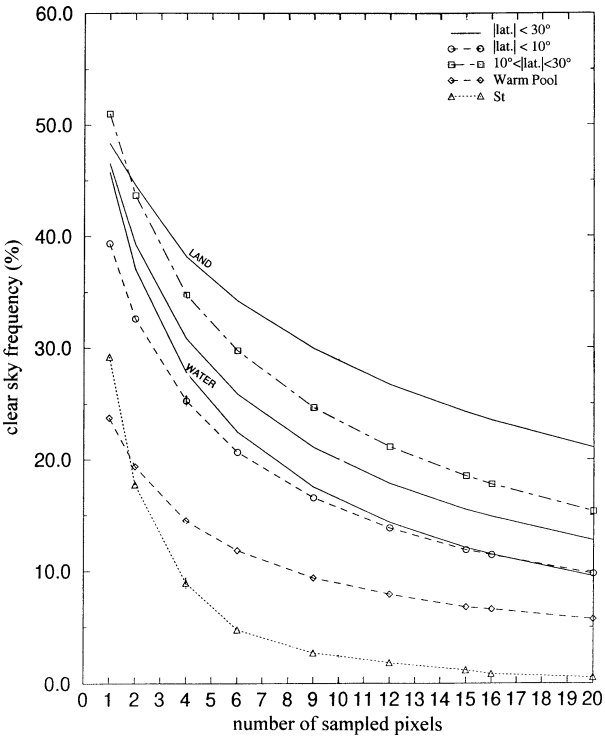

FIG. 9. Evolution of clear-sky frequency as a function of pixel size. Pixel size is simulated by adjacent ISCCP grid boxes from AVHRR measurements on *NOAA-12*. Results are shown for different geographical regions: the lat band between −30° and +30° for all scenes and for land and ocean separately, the Tropics (lat between −10° and +10°), NH subtropics (lat between 10° and 30°), the convection zone over Indonesia (Warm Pool), and stratocumulus regions (St).

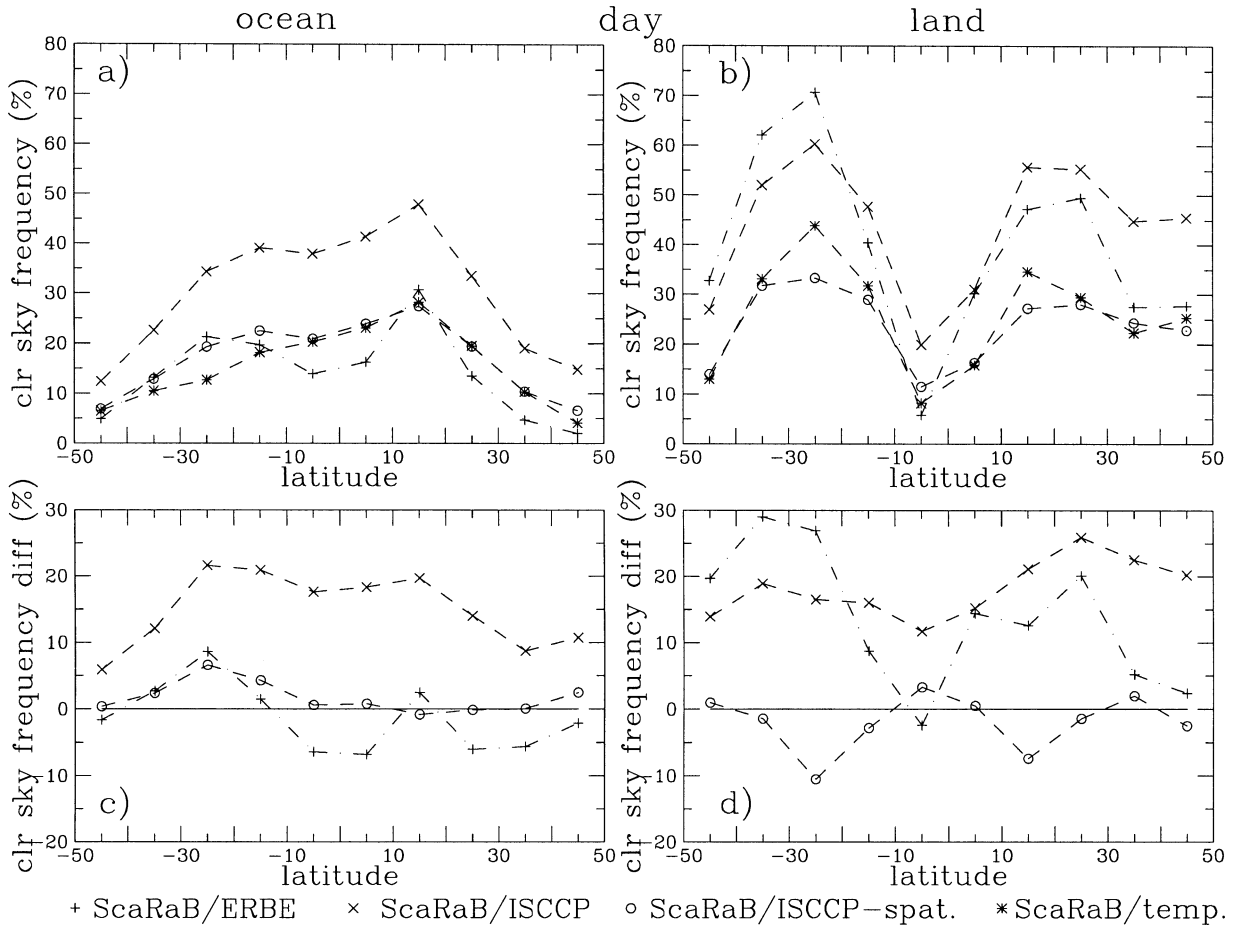

FIG. 10. Zonally averaged clear-sky frequency at ScaRaB pixel resolution from ERBE identification (ScaRaB–ERBE), original ISCCP (ScaRaB–ISCCP), ScaRaB spatial resolution–adapted ISCCP identification (ScaRaB–ISCCP-spat.), and ScaRaB local time sampling–adapted method (ScaRaB–temp.) (a) over ocean and (b) over land, with differences resulting from the first three methods and method 4 (c) over ocean and (d) over land. Statistics are from daytime measurements in Mar 1994.

fication as the basis for the time sampling–adapted ISCCP clear-sky identification, these two methods are quite independent, because the latter uses time statistics whereas the former uses regional statistics of the same geotype for the determination of the clear-sky composites. This new clear-sky identification method is then applied to the ScaRaB data of March 1994 and results are shown in the following sections.

3. Clear-sky frequencies and clear sky TOA LW fluxes

a. Clear-sky frequencies and LW fluxes at pixel resolution

To get a first impression of the original ISCCP clear-sky identification over ScaRaB pixels, we compare in Fig. 8 the resulting zonal mean clear-sky frequencies (ScaRaB–ISCCP) with those obtained by the ERBE inversion (ScaRaB–ERBE) and with clear-sky frequencies from ISCCP data (AVHRR–ISCCP). For this study we use quasi-simultaneous ScaRaB and AVHRR data covering the period from 24 to 26 March 1994 (see section 2c).

From Fig. 8 one notices first that the ERBE clear-sky frequency is systematically the smallest: especially in the Tropics the difference between ERBE and ISCCP reaches 20%. The difficulty of finding clear sky in the tropical regions with the ERBE algorithm can be explained by the fact that the broadband channels are also sensitive to water vapor, which is interpreted as thin cloud. On the other hand, the clear-sky frequency found with the ISCCP algorithm applied to the ScaRaB pixels is quite close to that observed over the sampled AVHRR pixels (section 2b), varying from 35% in the Tropics to 55% in the desert regions. The average clear-sky frequencies for ScaRaB–ISCCP are only about 5% smaller than for AVHRR–ISCCP, even though the ScaRaB pixel size is much larger than the area covered by the AVHRR pixels sampled to a 0.25° grid.

The clear-sky frequency expected over a region of the size of ScaRaB pixels can be estimated by simulating the ScaRaB pixels by an accumulation of four adjacent

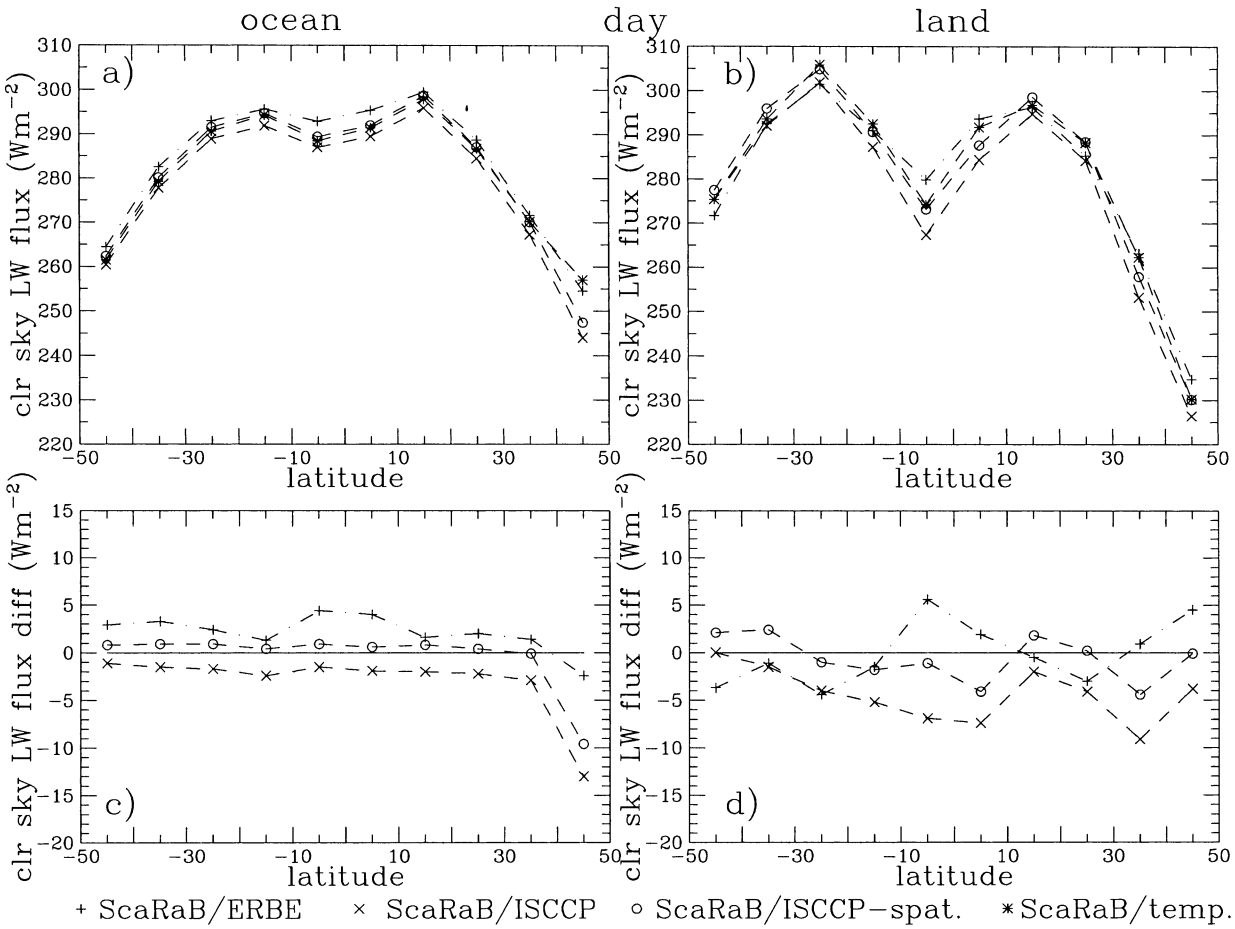

FIG. 11. Same as Fig. 10, but for zonally averaged clear-sky LW fluxes at TOA.

ISCCP grid boxes (Fig. 1). A composite of adjacent gridboxes will be declared clear only if all AVHRR pixels are clear. Since the AVHRR pixels are sampled and small clouds hide just in the regions between the sampled AVHRR pixels, as illustrated in Fig. 1, the simulated ScaRaB clear-sky frequency could be slightly overestimated. The evolution of clear-sky frequency with increasing region of observation (increasing number of merged ISCCP grid boxes) is presented in Fig. 9. From this figure, one concludes that the clear-sky frequency over ScaRaB pixels should be on average about 15% smaller than the clear-sky frequency over one ISCCP gridbox. One notices that this evolution varies strongly with the observed region: in regions with clouds of large extent, like in the deep convection zone over Indonesia (''Warm Pool''), the difference is only 10%; whereas in regions with small stratocumulus clouds (''St''), one finds a decrease of clear-sky frequency of about 20%. The fact that only a 5% smaller clear-sky frequency is observed in Fig. 8 shows, on one hand, a certain stability of the ISCCP cloud detection with spatial resolution, because the general cloud amount is about the same, regardless of which measurement is used. On the other hand, this stability implies more cloud contamination of the clear radiances. For a clear-sky identification without cloud contamination over ScaRaB pixels, as for the study of cloud radiative effects or for the development of ADMs, the test parameter values used at several places in the ISCCP algorithm have to be adjusted to the spatial resolution of the ScaRaB pixels as in section 2c.

Clear-sky frequencies, obtained from all four methods described in section 2, are compared for daytime measurements during the whole month of March 1994 in Fig. 10, separately for ocean and land. In order to facilitate the comparison, differences are also shown between the first three methods and the fourth method. By adapting the ISCCP method to the spatial resolution of the ScaRaB pixels, the clear-sky frequency has been reduced in general by about 5%–20%, in agreement with the simulation shown in Fig. 9. The clear-sky identification method developed for the temporal sampling of ScaRaB gives results similar to the ISCCP method adapted to the spatial resolution of the ScaRaB pixels. This indicates that the consideration of seasonal shifts of clear-sky temperatures included in the original ISCCP

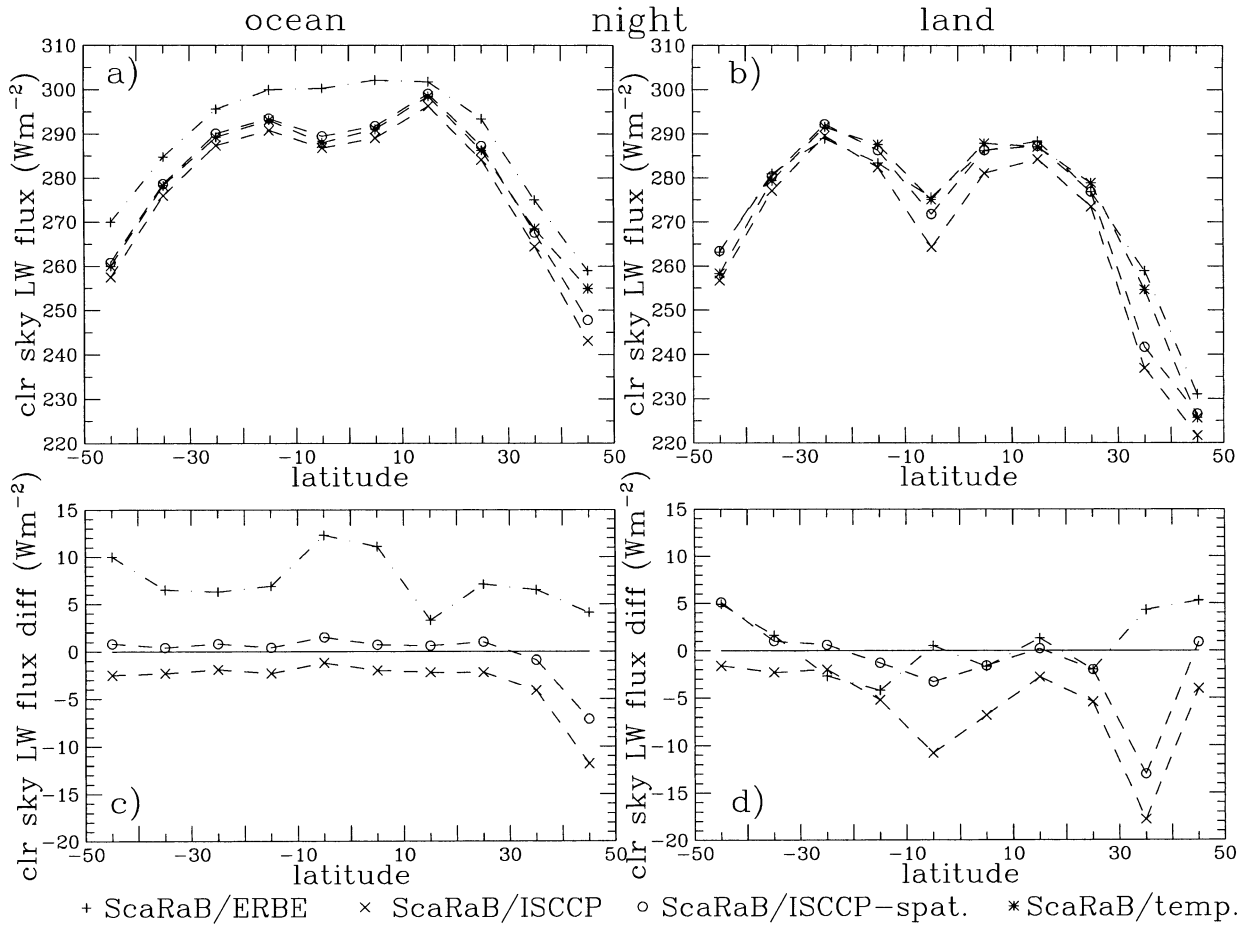

FIG. 12. Same as Fig. 11, but for nighttime measurements in Mar 1994.

algorithm also works well for the temporal shift at ScaRaB scale. Nevertheless, the clear-sky frequency has been slightly increased in regions with a strong diurnal cycle (subtropical land). The ERBE identification still yields the smallest clear-sky frequency over ocean, especially in the Tropics, where the water-vapor abundance is high. Over land the situation is different, because ERBE detects about 20% more clear sky in the subtropics where most of the deserts are. The other clear sky identifications, which are based more on spatial and temporal variability than on the warmest and darkest scenes, detect less clear sky in these regions. The results for nighttime measurements (not shown) are similar, with an even lower ERBE clear-sky frequency over ocean, which leads to a difference in the Tropics of 20%.

On the other hand, the clear-sky LW fluxes (Fig. 11 for day and Fig. 12 for nighttime measurements), obtained from all four methods described in section 2, are more similar. The original ISCCP clear-sky identification yields the lowest LW fluxes, and ERBE the highest LW fluxes. The difference in general is around 5 W m^{-2}. In the Tropics and during night, however, the difference can exceed 10 W m^{-2}, indicating that the use of the narrowband channels probably leads to a more reliable scene identification. Note that the oceanic clear-sky fluxes are not expected to change much from day to night (but the ERBE method yields higher nighttime clear-sky fluxes); whereas, clear-sky fluxes in the dry subtropical zones are 10–15 W m^{-2} smaller during night than during daytime. Over subtropical land in the Southern Hemisphere, the ERBE algorithm identifies deserts as nearly always cloud-free and yet produces a 5 W m^{-2} lower clear-sky LW flux than the method that accounts for the different ScaRaB temporal sampling. From Fig. 11 and Fig. 12 we also deduce that the adjustment of the ISCCP cloud detection to ScaRaB spatial resolution has a smaller effect on the clear-sky LW fluxes than on the clear-sky frequency. Even if the clear-sky frequency has been reduced by 10%–20%, taking out most scenes with residual cloud contamination, the clear-sky fluxes increase by only 2 W m^{-2} over ocean and up to 8 W m^{-2} over tropical land. Note that over ocean the method that accounts for the different ScaRaB temporal sampling gives nearly identical results to the spatial resolution–adapted ISCCP method, whereas differences over land are about 3 W m^{-2}. Standard deviations of

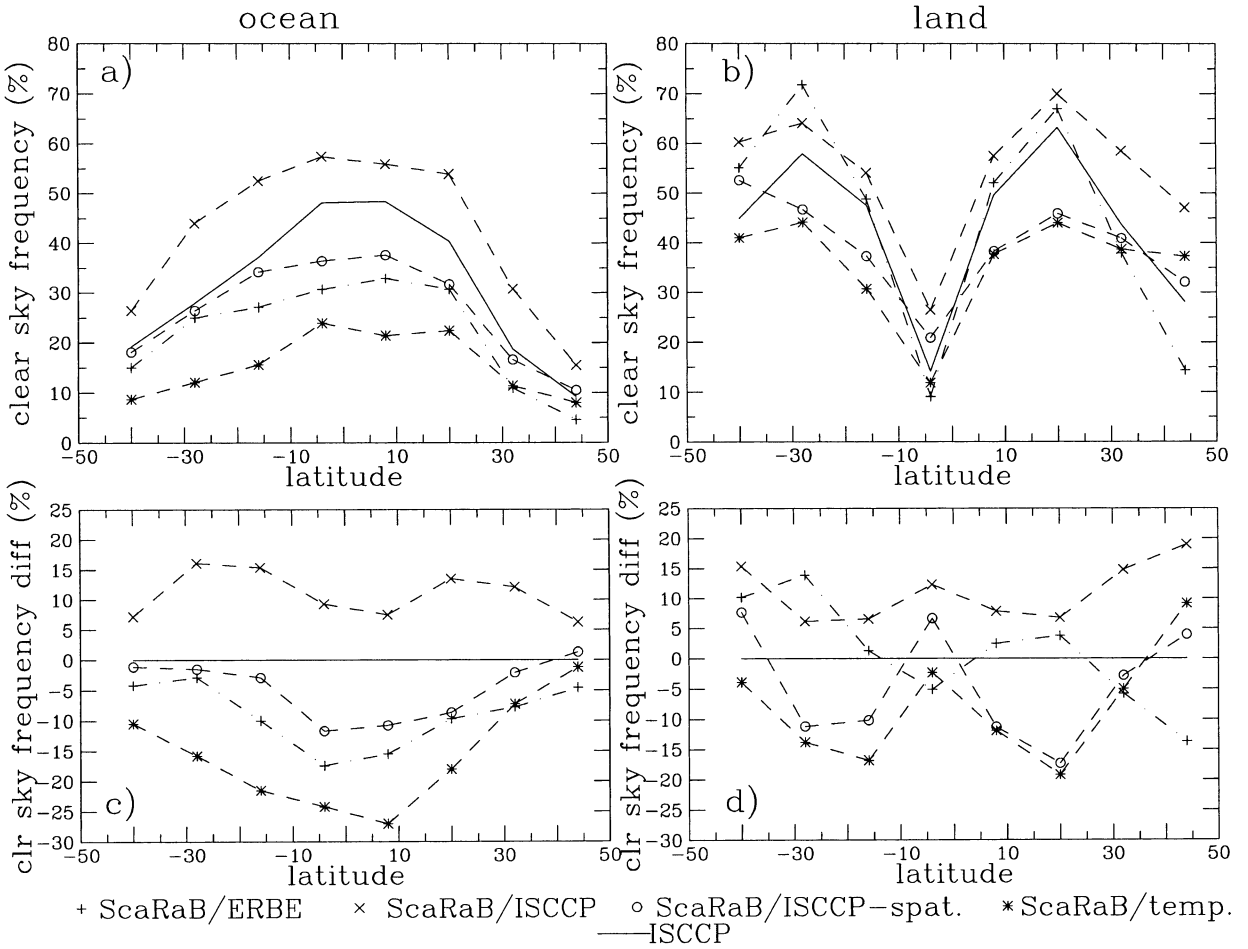

FIG. 13. Same as Fig. 10, but at GCM spatial resolution, compared with collocated ISCCP clear-sky scenes (ISCCP). The clear-sky frequency corresponds to the fraction of 4° × 5° regions, which have clear sky extending over at least a 1° × 1° region. Differences between the four methods applied to ScaRaB and collocated ISCCP clear-sky are also shown (c) for ocean and (d) for land.

the zonally averaged clear-sky fluxes are around 10–15 W m^{-2} over land and less than 10 W m^{-2} over ocean, slightly smaller for the newly developed method.

b. Clear-sky frequencies and LW fluxes at general circulation model (GCM) spatial resolution

For a further evaluation of the cloud detection methods described in section 2, the ScaRaB data have been combined with simultaneous (within 15 min) observations from the ISCCP data. The ISCCP data are organized on a grid of 0.25°, as compared with 0.33° for the ScaRaB data. Therefore, for the collocation, each dataset has been degraded to 1°. Since the coordinates of the ScaRaB pixels are given, as for ERBE pixels, at TOA, they had to be transformed to the surface coordinates used by ISCCP. The coordinate transformation, which depends on the viewing zenith angle, affects the instantaneous LW fluxes by up to 2 W m^{-2} and the SW fluxes by up to 10 W m^{-2} (Stubenrauch et al. 1999). Fluxes have been averaged over the 1° × 1° grid, whereas cloud and surface properties have been respectively averaged over cloudy and clear-sky pixels. A 1° × 1° grid is declared as clear-sky when all pixels are clear. Another difficulty in the collocation process is that the exact observation time is not kept in the ISCCP climatology. For this reason we could collocate only daytime measurements, because the solar zenith angle could be used as a measure of observation time. This collocated dataset was created for the development of SW ADMs (Briand 2000).

The probability of clear sky extending over a region of 1° × 1° is only about two-thirds as high as over 60 km × 60 km regions (Fig. 9) and thus the problem of low sample populations is aggravated. On the other hand, clear sky over larger regions consisting of several pixels detected as clear-sky is probably more reliable than regions of one pixel. A sensitivity analysis can be done by first averaging the 1° clear-sky fluxes over regions of 4° × 5° (the spatial resolution of many climate GCMs) and then calculating the zonal means. In this way, the weight between regions of low cloudiness and

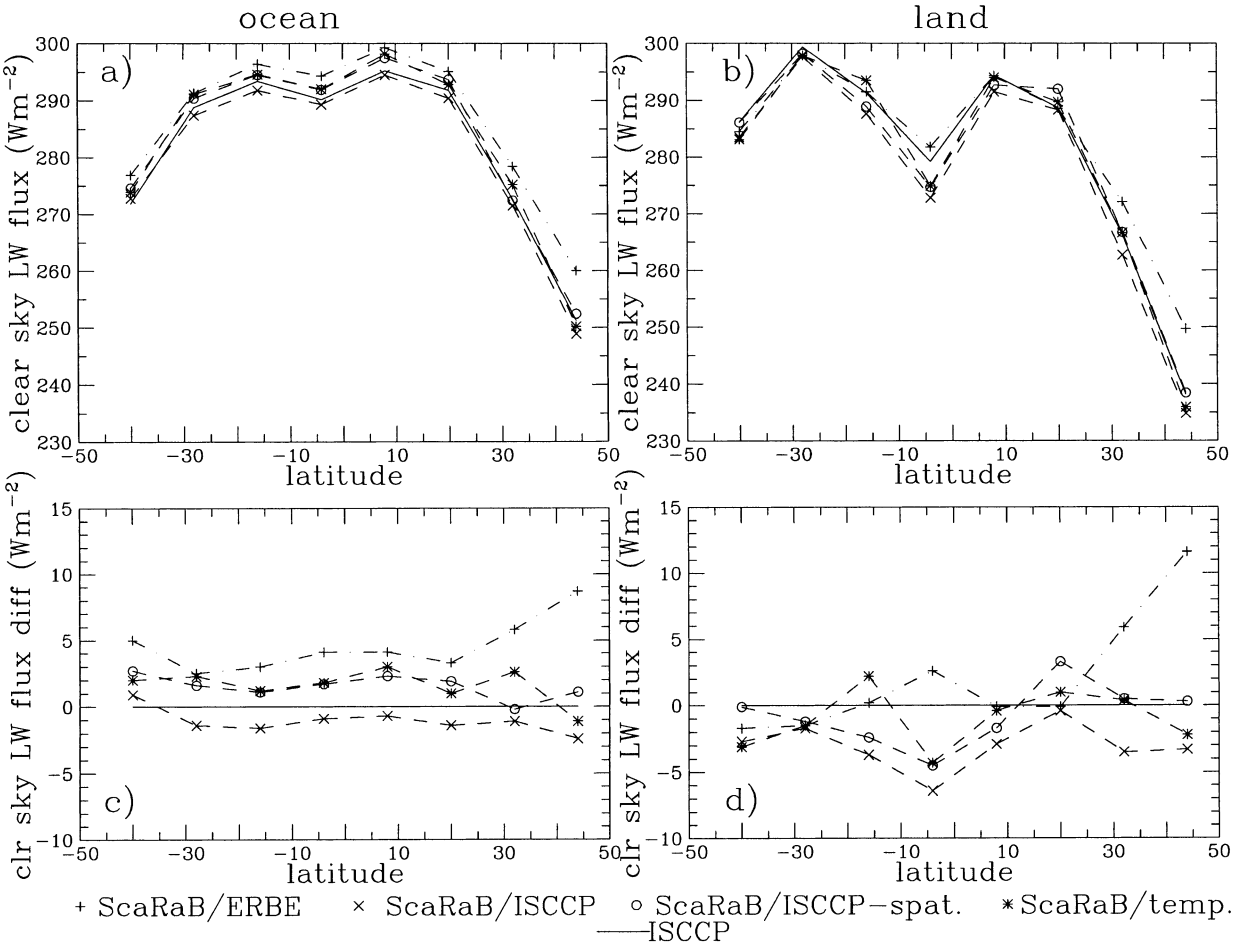

FIG. 14. Same as Fig. 13, but for clear-sky outgoing LW fluxes at TOA. One-degree clear-sky fluxes are first averaged over regions of 4° × 5°. Clear-sky flux differences between the four methods applied to ScaRaB and ScaRaB fluxes from collocated ISCCP clear sky are also shown (c) for ocean and (d) for land.

regions of high cloudiness will be more equal. This should give more stable results, especially in regions with low clear-sky frequencies. In addition, these results can be more directly compared with results from GCMs, since these quantities can be computed in the same manner. The clear-sky frequency then corresponds to the fraction of 4° × 5° regions that have clear sky extending over at least one 1° × 1° region.

Figure 13 presents the frequency of 4° × 5° regions with clear sky extending over at least 1° × 1°, determined from ScaRaB data using the four cloud detection methods described in section 2, in comparison with results from the time–space-collocated ISCCP data. Results are shown for daytime measurements in March 1994, separately for ocean and land. Again, differences are also shown for easier comparison.

Considering ocean, the largest clear-sky frequency is found by the original ISCCP cloud detection applied to ScaRaB data, indicating a residual cloud contamination. The clear-sky frequency from the ISCCP data is about 5%–10% lower, but note that because of the sampling some clouds could be hidden, so this clear-sky frequency estimate should be an upper limit for the comparison with clear sky for ScaRaB pixels. The frequencies from the spatial resolution–adapted ISCCP cloud detection and from the ERBE algorithm are close and 5%–10% lower than the result from ISCCP data, with a larger difference in the Tropics where clear-sky regions are probably smaller. Note that this time the lowest clear sky frequencies come from the newly developed ScaRaB cloud detection, which determines clear-sky composites from regional statistics. The comparison of Fig. 13 and Fig. 10 indicates that this method yields smaller clear-sky regions over ocean than the ERBE method.

Over land, the tendencies are the same, with the exception of the desert zones where ERBE finds the most clear sky and the difference between original ISCCP and the ScaRaB-adapted cloud detections are larger due to broken cloudiness. Note that the clear-sky frequency of the newly developed ScaRaB cloud detection is much closer again to the ISCCP threshold-adapted method than over ocean.

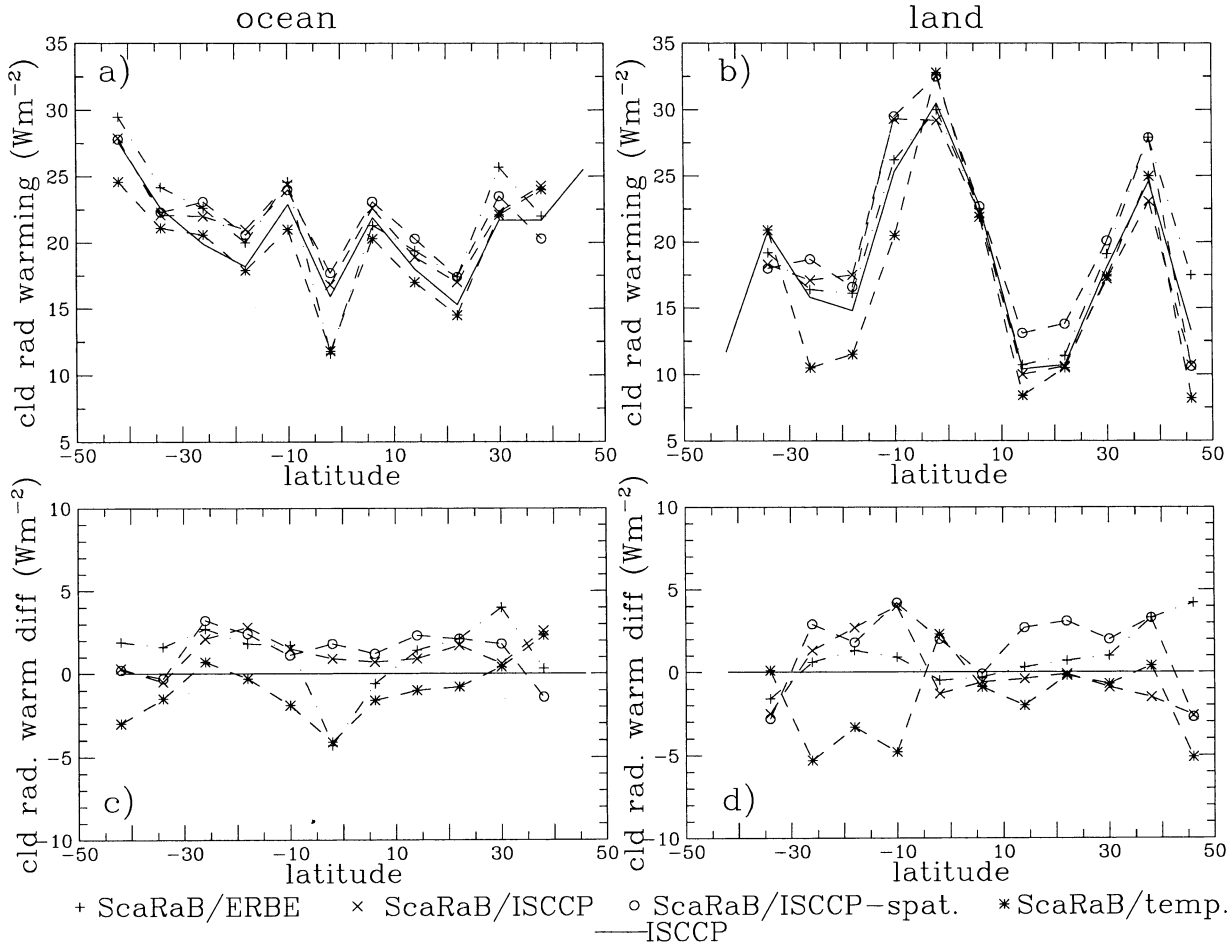

FIG. 15. Same as Fig. 14, but for cloud radiative warming.

Figure 14 shows the zonal mean LW fluxes from 1° × 1° clear-sky regions and averaged over 4° × 5° regions, together with differences. In the case of ISCCP data, the ScaRaB LW fluxes are associated with collocated 1° × 1° clear-sky scenes detected in the ISCCP data. Over ocean, zonal LW fluxes corresponding to ERBE clear sky are in general about 5 W m^{-2} higher than those obtained from the original ISCCP identification, the latter close to fluxes corresponding to clear-sky regions from ISCCP data. The algorithms adjusted to ScaRaB spatial and temporal resolution identify clear sky that is less contaminated with clouds and therefore produce slightly larger LW fluxes (by about 2–3 W m^{-2}). The situation over land looks similar to that in Fig. 11. Note that at Northern Hemisphere midlatitudes the zonal mean clear sky LW flux is 5–10 W m^{-2} higher for ERBE than for ScaRaB. In these regions, the sun is just rising, the mean solar zenith angle is larger than 63°, and the ERBE clear sky frequencies are also small. The difference between Figs. 14 and 11 could be explained by these effects.

4. Cloud radiative effects

a. Cloud radiative warming

As mentioned in section 1, a first estimate of the radiative warming effect of clouds can be obtained by analyzing the difference between the monthly averaged clear-sky LW flux and the total LW flux for each region at TOA. This global cloud radiative warming effect takes into account the occurrence of clouds as well as variations of their physical properties like physical size, thickness and height. Since with observations one can only sample clear sky when clouds do not occur (Cess and Potter 1987; Harshvardan et al. 1989), changes in the atmospheric state that are correlated with cloud occurrence are included in the determination of ''cloud'' radiative effects from satellite observations. In this section we are interested in results that can be directly compared to GCMs. Therefore we use, as in section 3b, statistics over regions of 4° × 5°. Only regions are used for this analysis, which have at least one 1° × 1° grid completely filled with clear-sky pixels. Figure 15 presents the cloud radiative warming as obtained from

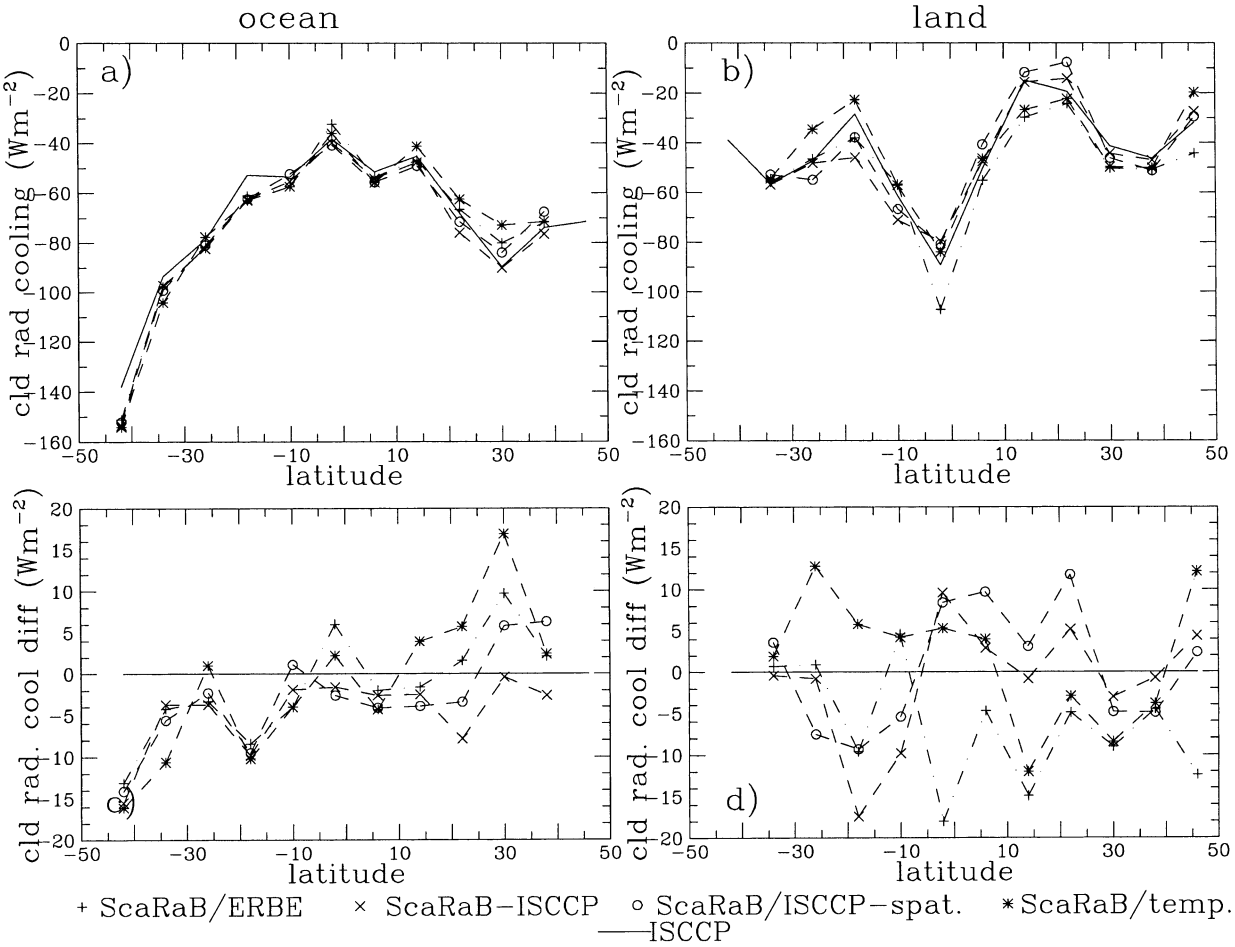

FIG. 16. Same as Fig. 14, but for cloud radiative cooling.

ScaRaB data for March 1994 during daytime (morning satellite pass), separately over land and ocean. Only results using statistics of more than 10 points are shown. As in section 3, results from the different clear-sky identifications are compared. During March 1994 the ScaRaB observation time shifts from 1030 LST to 0630 LST. The cloud radiative warming is the highest over tropical land, where it reaches 30 W m^{-2}, and 23 W m^{-2} over tropical ocean. The intertropical convergence zone, with its frequent occurrence of high opaque clouds, is responsible for this effect. In the subtropics where clouds occur less often and are lower and thinner, the cloud radiative warming is only about 10 W m^{-2} over land, but 15 W m^{-2} over ocean where there are more persistent stratocumulus regions.

Since, in Fig. 14 over ocean, the ERBE clear-sky LW fluxes are systematically higher than the ones obtained from the ISCCP cloud detection, one would expect a slight overestimation of the cloud radiative warming effect when determined by using the ERBE clear-sky identification. However, if one compares Fig. 15 with Fig. 14, the correlation is not straightforward, since an additional uncertainty comes from the different clear-sky sampling, especially in regions where clear sky does not appear often. The difference between clear-sky flux and total flux can only be determined for regions where there was at least one clear-sky occurrence during the month of March. If these regions are not the same within one latitude zone when using different clear-sky identifications, such a difference in sampling adds another uncertainty in determining the cloud radiative effects. Around the equator, where the ERBE clear-sky fluxes are about 4 W m^{-2} higher, the cloud warming can be lower or equal to the one found in combination with ISCCP data. This can only be explained by the fact that the clear-sky scenes found by ERBE are preferentially located in regions where there is less cloudiness. It is interesting to note that the two methods developed for ScaRaB (described in sections 2c and 2d) lead to very similar clear-sky fluxes over ocean (Fig. 14), but show systematic differences of cloud warming of about 3 W m^{-2}. The cloud radiative warming is stronger when clear sky is found by the ScaRaB spatial resolution–adapted ISCCP cloud detection. This indicates that, by replacing the time statistics with space statistics (within the same geotype) over a smaller time period, clear sky is found

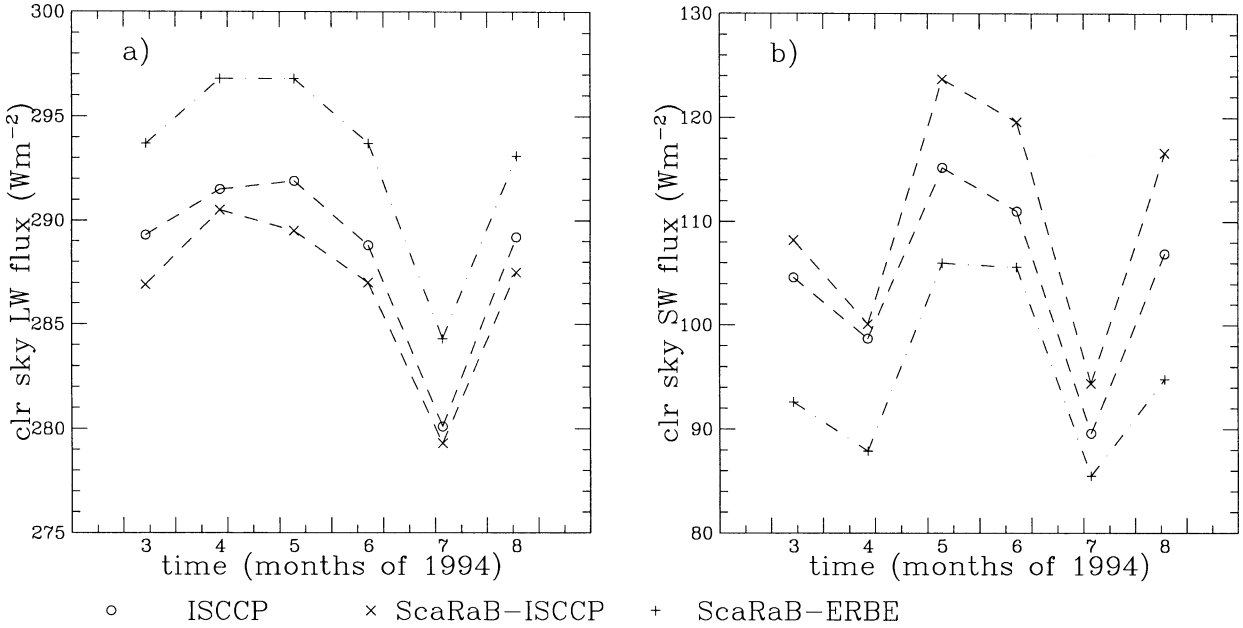

FIG. 17. Outgoing clear-sky fluxes in the Tropics (lat band from 14°N to 14°S) as a function of ScaRaB observation month, (a) LW and (b) SW. Clear sky over a ScaRaB pixel is identified by ERBE (ScaRaB–ERBE), original ISCCP (ScaRaB–ISCCP), compared with fluxes for collocated ISCCP clear-sky scenes (ISCCP). Statistics from regions of 4° × 5° are considered during daytime.

more often in regions with smaller cloud amounts. Over land, this effect can be seen in the Southern Hemisphere, where the last method estimates a 5 W m^{-2} smaller cloud warming than all other methods.

b. Cloud radiative cooling

Cloud radiative cooling is also examined. Since the SW fluxes depend strongly on the sun elevation and the ScaRaB observation time changes considerably over 1 month, the SW cooling effect is more difficult to analyze. Clear sky SW albedos (not shown) are between 11% and 17% over ocean and between 15% and 25% over land. Similar effects, as for the clear-sky LW fluxes, are produced by the different clear-sky detection methods. Over ocean, the ERBE clear-sky albedo is systematically the lowest, whereas it is highest in the desert regions and over tropical land. Again, the ScaRaB-

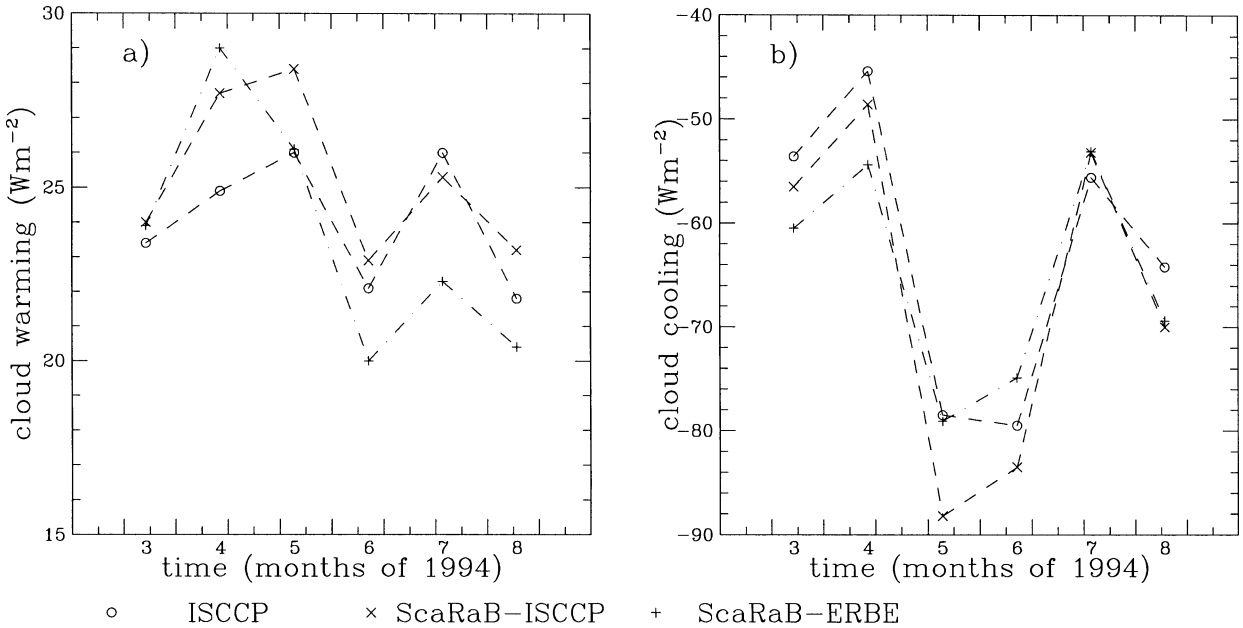

FIG. 18. Same as Fig. 17, but for (a) cloud radiative warming and (b) cloud radiative cooling.

adapted clear-sky identifications yield scenes with less cloud contamination (lowest clear-sky albedo). The radiative cloud cooling in the morning, which is the difference between clear-sky SW flux and total SW flux, is presented in Fig. 16. The mean observation time increases slightly from the Northern Hemisphere (mean solar zenith angle 65° at 45°N) to the Southern Hemisphere (mean solar zenith angle 55° at 45°S). The strongest radiative cooling effect of about 90 W m^{-2} is seen in the Tropics over land (also with the strongest warming effect), indicating that the intertropical convergence zone (ITCZ) is situated mostly over land in March. Another region of strong cloud cooling can be observed over Southern Hemisphere midlatitude oceans, indicating frequent storms and thick low-level clouds. The effect of sampling statistics due to different clear-sky identification plays a much smaller role over ocean (differences of about 5 W m^{-2} with the exception of Northern Hemisphere subtropics where differences range up to 20 W m^{-2}) than over land. The ERBE-like analysis gives a 20 W m^{-2} stronger cloud cooling over tropical land than all other clear-sky identifications. This shows again that clear-sky statistics are an important uncertainty factor in determining cloud radiative effects.

c. Cloud radiative effects in the Tropics

To finalize our sensitivity study, we show in Fig. 17 tropical (latitude band between 14°N and 14°S) outgoing LW and SW fluxes for clear-sky determined by the original ISCCP and ERBE algorithms applied to ScaRaB data and from the ISCCP data for 6 months of collocated ScaRaB–ISCCP daytime data. The tropical differences between ERBE clear-sky identification and the newly developed ScaRaB methods using the narrow-band channels have been identified in section 3 as the largest, because the Tropics have the highest water-vapor abundance. As mentioned in the introduction, the observation time of the *Meteor* satellite changes during the months: daytime observations were taken around 0800 LST in March, 1700 LST in April, 1400 LST in May, 1100 LST in June, 0800 LST and 1800 LST in July, and 1500 LST in August. Sun zenith viewing angles vary between 60° (in July) and 35° (in May and June). Since the seasonal variation of clear-sky temperature in the Tropics is small, the variation of the clear-sky fluxes as a function of observation month are most probably caused by diurnal variation. From Figs. 17a and 17b one concludes that, at all these observation times, the ERBE clear-sky LW fluxes are systematically 4 W m^{-2} higher and the SW fluxes 5–10 W m^{-2} lower than the ones obtained from ISCCP clear sky. On the other hand, as seen in the sections before, the clear-sky identification from the original ISCCP algorithms on the ScaRaB data is slightly cloud contaminated leading to about 1 W m^{-2} lower LW fluxes and to 5–10 W m^{-2} higher SW fluxes than those from ISCCP clear sky. Assuming the same total fluxes, one would obtain the strongest cloud warming effect and strongest cloud cooling effect using the ERBE clear-sky identification. By investigating the tropical cloud radiative effects in Figs. 18a and 18b, one observes again that this conclusion is not generally applicable. It is only true in the first 3 months, whereas the effect is the opposite in the second 2 months where fewer cloudy regions have been picked out to represent clear-sky statistics. This means that on a monthly basis the uncertainty due to different clear-sky statistics adds another 4-W m^{-2} uncertainty for the cloud warming and 5 W m^{-2} for the cloud cooling effect.

5. Conclusions

Different cloud detection methods making use of the narrowband channels of the ScaRaB radiometer allow for a sensitivity study on zonally averaged clear-sky fluxes at TOA and on cloud radiative effects compared to results using the ERBE clear-sky identification. We have seen that the ERBE method produces systematically higher clear-sky LW fluxes (2–10 W m^{-2}) than the ISCCP clear-sky identification adapted to ScaRaB spatial resolution and to temporal sampling. The latter are close to (about 1 W m^{-2} higher) fluxes corresponding to clear-sky regions from ISCCP data. Employing the original ISCCP cloud detection on the ScaRaB data shows already that the narrowband channels are very useful for cloud detection, but residual cloud contamination leads to 1–2 W m^{-2} lower clear-sky LW fluxes than those corresponding to ISCCP clear sky. Especially in the Tropics where water vapor is abundant, the ERBE clear-sky fluxes seem to be systematically overestimated by about 4 W m^{-2}, and SW fluxes are lower by about 5–10 W m^{-2}. However, the determination of cloud radiative effects from flux observations in this manner depends not only on the value of clear-sky fluxes but also on clear-sky sampling statistics. Whereas clear-sky fluxes of the two ScaRaB-adapted clear-sky identifications are very close, their cloud radiative warming and cooling can still differ by 5 and 10 W m^{-2}, respectively. On average, the uncertainty due to different clear-sky statistics increases the cloud warming and cloud cooling uncertainties by another 4 and 5 W m^{-2}, respectively.

REFERENCES

Barkstrom, B. R., and Coauthors, 1989: Earth Raditation Budget Experiment (ERBE) archival and April 1985 results. *Bull. Amer. Meteor. Soc.,* **70,** 1254–1262.

Briand, V., 2000: Towards a better exploitation of satellite observations for the study of cloud radiative effects. Ph. D. dissertation, University of Paris VI, 129 pp. [Available in French from LMD, Ecole Polytechnique, F-91128 Palaiseau cedex, France.]

Capderou, M., 1995: One year of ScaRaB: Orbits and temporal sampling of the *Meteor 3-07* satellite. LMD Tech. Note 199, 250 pp. [Available in French from LMD, Ecole Polytechnique, F-91128 Palaiseau cedex, France.]

Cess, R. D., and G. L. Potter, 1987: Exploratory studies of cloud radiative forcing with a general circulation model. *Tellus,* **39A,** 460–473.

Charlock, T. P., and V. Ramanathan, 1985: The albedo field and cloud radiative forcing produced by a general circulation model with internally generated cloud optics. *J. Atmos. Sci.,* **42,** 1408–1429.

Chen, T., W. B. Rossow, and Y.-C. Zhang, 2000: Radiative effects of cloud type variations. *J. Climate,* **13,** 264–286.

Collins, W. D., and A. K. Inamdar, 1995: Validation of clear-sky fluxes for tropical oceans from the Earth Radiation Budget Experiment. *J. Climate,* **8,** 569–578.

Harrison, E. F., P. Minnis, B. R. Barkstrom, V. Ramanathan, R. D. Cess, and G. G. Gibson, 1990: Seasonal variation of cloud radiative forcing derived from the Earth Radiation Budget Experiment. *J. Geophys. Res.,* **95,** 18 687–18 703.

Harshvardhan, D. A. Randall, T. G. Corsetti, and D. A. Dazlich, 1989: Earth radiation budget and cloudiness simulations with a general circulation model. *J. Atmos. Sci.,* **46,** 1922–1942.

Hartmann, D. L., and D. Doelling, 1991: On the net radiative effectiveness of clouds. *J. Geophys. Res.,* **96,** 869–891.

Kandel, R., and Coauthors, 1998: The ScaRaB earth radiation budget dataset. *Bull. Amer. Meteor. Soc.,* **79,** 765–783.

Ockert-Bell, M. E., and D. L. Hartmann, 1992: The effect of cloud type on earth's energy balance: Results for selected regions. *J. Climate,* **5,** 1158–1171.

Ridout, J. A., B. Chertock, and R. Gelaro, 1994: Response of a general circulation model to a change in cloud solar forcing: Model feedbacks and comparison with satellite data. *J. Geophys. Res.,* **99,** 18 555–18 576.

Rossow, W. B., and R. A. Schiffer, 1991: ISCCP cloud data products. *Bull. Amer. Meteor. Soc.,* **72,** 2–20.

——, and L. C. Garder, 1993a: Cloud detection using satellite measurements of infrared and visible radiances for ISCCP. *J. Climate,* **6,** 2341–2369.

——, and ——, 1993b: Validation of ISCCP cloud detections. *J. Climate,* **6,** 2370–2393.

——, and Y.-C. Zhang, 1995: Calculation of surface and top of atmosphere radiative fluxes from physical quantities based on ISCCP datasets. 2. Validation and first results. *J. Geophys. Res.,* **100,** 1167–1197.

——, and R. A. Schiffer, 1999: Advances in understanding clouds from ISCCP. *Bull. Amer. Meteor. Soc.,* **80,** 2261–2287.

——, L. C. Garder, and A. A. Lacis, 1989: Global, seasonal cloud variations from satellite radiance measurements. Part I: Sensitivity of analyses. *J. Climate,* **2,** 419–458.

Rutan, D. A., and T. P. Charlock, 1997: Spectral reflectance, directional reflectance and broadband albedo of the earth's surface. Preprints, *Ninth Conf. on Atmospheric Radiation,* Long Beach, CA, Amer. Meteor. Soc., 446–470.

Sèze, G., and W. B. Rossow, 1991: Effects of satellite data resolution on measuring the space/time variations of surfaces and clouds. *Int. J. Remote Sens.,* **12,** 921–952.

Smith, G. L., R. N. Green, E. Raschke, L. M. Avis, J. T. Suttles, B. A. Wielicki, and R. Davies, 1986: Inversion method for satellite studies of the earth's radiation budget: Development of algorithms for the ERBE mission. *Geophys. Rev.,* **24,** 407–421.

Stephens, G. L., and T. J. Greenwald, 1991: The earth's radiation budget and its relation to atmospheric hydrology. 2. Observations of cloud effects. *J. Geophys. Res.,* **96,** 15 325–15 340.

Stubenrauch, C. J., G. Seze, N. A. Scott, A. Chédin, M. Desbois, and R. S. Kandel, 1996: Cloud field identification for earth radiation budget studies. Part II: Cloud field classification for the ScaRaB radiometer. *J. Appl. Meteor.,* **35,** 428–443.

——, A. D. Del Genio, and W. B. Rossow, 1997: Implementation of subgrid cloud vertical structure inside a GCM and its effect on the radiation budget. *J. Climate,* **10,** 273–287.

——, W. B. Rossow, N. A. Scott, and A. Chédin, 1999: Clouds as seen by infrared sounders (3I) and imagers (ISCCP). Part III: Spatial heterogeneity and radiative effects. *J. Climate,* **12,** 3419–3442.

Viollier, M., R. S. Kandel, and P. Raberanto, 1995: Inversion and space–time averaging algorithms for ScaRaB (Scanner for Earth Radiation Budget)—Comparison with ERBE. *Ann. Geophys.,* **13,** 959–968.

Wielicki, B. A., and R. N. Green, 1989: Cloud identification for ERBE radiative flux retrieval. *J. Appl. Meteor.,* **28,** 1133–1146.

——, and L. Parker, 1992: On the determination of cloud cover from satellite sensors: The effect of sensor spatial resolution. *J. Geophys. Res.,* **97,** 12 799–12 823.